Microstructure, martensitic transformation kinetics, and magnetic properties of $(Ni_{50}Mn_{40}In_{10})_{100-x}Co_x$ melt-spun ribbons

Ahlem Bekhouche[1] · Safia Alleg[1] · Karima Dadda[1] · Mourad Ibrahim Daoudi[1,2] · Joan Saurina[3] · Joan-Josep Suñol[3]

Abstract

The effect of Co-doping on the structure, microstructure, martensitic phase transformation kinetics, and magnetic properties of the melt-spun $(Ni_{50}Mn_{40}In_{10})_{1-x}Co_x$ (x = 1, 2, and 3) Heusler ribbons, named hereafter Co1 (x = 1), Co2 (x = 2), and Co3 (x = 3), was assessed using X-ray diffraction, scanning electron microscope, energy-dispersive spectroscopy, X-ray fluorescence, differential scanning calorimetry, and vibrating sample magnetometer. The XRD results reveal the formation of a 14M martensite structure alongside the face-centered-cubic (fcc) γ phase. The crystallite size ranges between 50 and 98 nm for the 14M martensite and from 9 to 16 nm for the γ phase. The mass fraction of the γ phase lies between 36.4 and 44.2%. Co-doping affects the lattice parameters and the characteristic temperatures (martensite start, martensite finish, austenite start, and austenite finish). The calculated activation energy values for the non-isothermal martensitic transformation kinetics are 257 kJ mol^{-1} and 135.6 kJ mol^{-1} for the Co1 and Co2, respectively. The produced ribbons show a paramagnetic behavior. The variation in the coercivity can be related to the crystallite size and mass fraction of the γ phase. The produced ribbons exhibit an exchange bias at room temperature that decreases with increasing the Co content.

Keywords Ni–Mn–In–Co Heusler alloys · Microstructure · Martensitic transformation · Kinetics · Magnetic properties

Introduction

Ni–Mn–Z (Z = Sb, Al, Ga, Sn, and In) alloys belong to the Heusler alloy family of intermetallic compounds with a specific crystal structure. Heusler alloys have gathered significant attention owing to their multifunctional properties, covering magnetic, shape memory, and magnetostructural characteristics [1–4]. These characteristics position them as promising contenders for diverse applications such as magnetic shape memory devices, magnetic refrigeration, and spintronic devices [5, 6]. Upon cooling, Ni–Mn–Z Heusler alloys undergo a first-order martensitic transition, transitioning from a high-temperature cubic austenite phase (A_{aust}) to a low-temperature-modulated or non-modulated martensite phase (M_{art}). The magnetic coupling is ferromagnetic (FM) in the high-temperature phase and exhibits short-range antiferromagnetic (AFM) behavior for Mn-rich compounds [7]. Additionally, in stoichiometric compositions like Ni_2MnZ, the Mn–Mn coupling prevails, while off-stoichiometric alloys showcase FM–AFM interactions, eventually dictating their magnetic properties. The majority of Heusler alloys undergo a second-order magnetic transition (SOMT) as they shift from a ferromagnetic (FM) to a paramagnetic state (PM) around the Curie temperature (T_C). This transition leads to a negative magnetic entropy change, recognized as the direct magnetocaloric effect (MCE). Additionally, these alloys experience a first-order magnetic phase transition near the martensitic phase, resulting in a positive magnetic entropy change known as the inverse magnetocaloric effect (IMCE) near the martensitic phase transformation [8–11].

The composition and preparation method can affect the crystal structure and physical properties of the Ni–Mn–In Heusler alloys. By tuning the alloy composition

✉ Safia Alleg
joanjosep.sunyol@udg.edu

[1] Laboratory of Magnetism and Spectroscopy of Solids (LM2S), Physics Department, Badji Mokhtar Annaba University, P.O. Box 12, 23000 Annaba, Algeria

[2] Department of Science of Matter, Faculty of Mathematics and Computer Science and Material Science, University 8 Mai 1945, 24000 Guelma, Algeria

[3] Department of Fisica, Girona University, Campus Montillivi, Girona, Spain

and understanding the underlying mechanisms governing the material's behavior, it is possible to develop advanced materials with improved functional properties and performance. Different preparation methods were employed to prepare the Heusler alloys depending on their composition, desired properties, and applications, such as induction melting [12], spark plasma sintering [13], laser ablation [14], and melt spinning [15]. The selection of the appropriate method is crucial for achieving the desired material characteristics due to its limitations. For the arc melting method, the constituent elements are melted in an inert gas atmosphere using an electric arc to obtain an ingot and then annealed to improve its homogeneity and crystallinity. The obtained ingot can be employed in the melt-spinning technique to generate ribbons in a metastable state characterized by a uniform chemical composition. Furthermore, the exceptionally rapid cooling rate of approximately 10^6 K s^{-1} facilitates the formation of a highly textured microstructure, inducing a modification in atomic order. Besides, the shape of the ribbons could be mainly used as sensors, actuators, and magnetocaloric devices [16, 17].

The Co addition to Ni–Mn–In alloys modifies the martensitic transformation temperature [18]. Ni–Mn–In and Ni–Mn–Ga alloys exhibit comparable chemical and morphological properties but different crystallographic and physical properties within a specific compositional range [19]. However, Ni–Mn–In alloys are an attractive alternative for practical applications compared to Ni–Mn–Ga, as indium is more cost-effective than gallium. However, brittleness poses a challenge for some applications that can be mitigated by incorporating Co [20]. The precipitation of dispersive secondary phases, achieved through Co substitution for Ni in Ni–Mn–In alloys, further enhances plasticity. However, this phase can be supressed or reduced by using certain preparation techniques. Quaternary Heusler alloys combining Ni, Mn, In, and Co (Ni–Mn–In–Co) exhibit potential for use in magnetically driven refrigerants and actuators due to their higher magnetic driving force and notable magnetocaloric effect (MCE) [21–24]. Additionally, they offer several advantages, including simple preparation, a high adiabatic temperature change in the low field, a barocaloric effect, a wide cooling span, cost-effectiveness, rare-earth-free composition, non-toxic element constitution, environmental friendliness, good oxidation resistance, and superior mechanical properties compared to intermetallic materials.

The partial substitution of cobalt for Ni, Mn, or In in the Ni–Mn–In alloys has been studied by many groups [20–22]. However, the addition of Co to the Ni–Mn–In alloys where Co atoms may replace Ni, Mn, or In atoms has not been reported. The objective of the current investigation is to explore the effect of the doping of a small amount of Co (~ 1, 2, and 3%) in $(Ni_{50}Mn_{40}In_{10})_{100-x}Co_x$ melt-spun ribbons on the microstructure, martensitic phase transformation, and martensitic transition kinetics. Various analytical techniques, including X-ray diffraction, scanning electron microscope (SEM), energy-dispersive spectroscopy (EDS), energy-dispersive X-ray fluorescence spectrometry (XRF), differential scanning calorimeter (DSC), and vibrating sample magnetometer (VSM), were used to examine the microstructure, morphology, elemental analysis, martensitic transformation kinetics, and magnetic properties.

Experimental procedure

Co-doped polycrystalline ribbons with nominal compositions of $(Ni_{50}Mn_{40}In_{10})_{100-x}Co_x$ with $x = 1, 2$, and 3, named hereafter Co1, Co2, and Co3, respectively, were prepared using arc melting and then melt spinning. Ingots with mass of approximately 5 g were prepared from high-purity (> 99.98%) nickel (Ni), manganese (Mn), indium (In), and cobalt (Co) elements obtained from Sigma Aldrich. The arc melting process was performed using a MAM-1 Buhler compact arc melter within a water-cooled copper crucible under an argon atmosphere. The ingots underwent four melting cycles to ensure better homogeneity. The ribbons were produced using an MSP10 melt-spinning system under an argon atmosphere (400 mbar). The process involved casting the molten material onto a polished surface of a copper wheel rotating at a linear speed of 40 m s^{-1}. The nozzle wheel distance was 3 mm, the orifice diameter 0.5 mm, and the injection pressure 500 mbar. The thickness, width, and length of the produced ribbons were 15 μm, 1.5 mm, and 2–3 cm, respectively.

Ribbons' morphology was observed with a scanning electron microscope (SEM) TESCAN operating at 20 kV coupled with energy-dispersive spectroscopy for the elemental analysis. The alloy structure was followed by X-ray diffraction (XRD) on a Brüker D8 Advance diffractometer in a (θ–2θ) Bragg Brentano geometry using a Cu-Kα radiation ($\lambda_{Cu} = 0.15405$ nm). The hysteresis loops at room temperature were measured with a vibrating sample magnetometer Lake Shore 7400 VSM. A differential scanning calorimeter DSC Q2000 was used to study the kinetics of the martensitic transformation in the dynamic mode under an argon atmosphere. The heating/cooling rates were 3, 5, 7, and 10 °C min^{-1} over the temperature domain from 200 to 450 °C, spanning the martensitic transformation. The chemical composition of the Heusler alloys was determined using an energy-dispersive X-ray fluorescence spectrometer (ED-XRF) on a Fisherscope XDV-SDD Helmut Fisher GmbH.
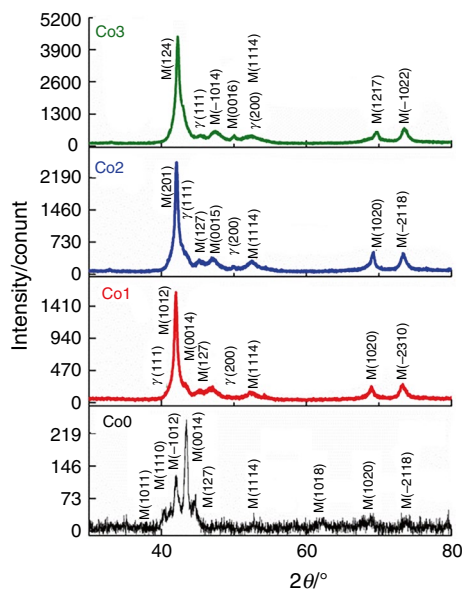
Fig. 1 XRD patterns of the $(Ni_{50}Mn_{40}In_{10})_{100-x}Co_x$ ($x = 0. 1. 2,$ and 3) Heusler alloys

Results and discussion

Structural characterization

Figure 1 illustrates the XRD patterns of the Co1, Co2, and Co3 Heusler ribbons with that of undoped $Ni_{50}Mn_{40}In_{10}$ for comparison. One observes that the intensity of the principal diffraction peak increases and broadens with increasing the Co content. As the atomic size of Co ($r_{Co} = 0.135$ nm) is equal to that of Ni ($r_{Ni} = 0.135$ nm) but smaller than that of Mn ($r_{Mn} = 0.140$ nm) and In ($r_{In} = 0.150$ nm), the Co addition to the NiMnIn alloy can affect its homogeneity and crystal structure, leading to changes in diffraction peak intensities and positions. The increase in the peak intensities can be related to the position of the cobalt atoms in the different sites that can modify the interatomic distances, the formation of the γ phase, and the increase in the crystallite size. The slight shift in the peak's position can be due to the lattice strains and the variation in the lattice parameters of the martensite structure. The XRD patterns were refined using the MAUD program [25] by introducing the monoclinic with a fourteen-layer-modulation14M martensite structure belonging to space group P21/m, the face-centered-cubic (*fcc*) γ phase, space group *Fm-3m*, for the Co1, Co2, and Co3 alloys, and only 14M martensite for the Co-free Heusler alloy (Fig. 2). The lattice parameters, average crystallite sizes, mass fractions, and reliability factors are gathered in Table 1. The Co-doping into the Ni–Mn–In Heusler alloys can affect their composition and electronic and magnetic properties, disturbing the stability of different phases and their balance. The *fcc* structure may be due to specific
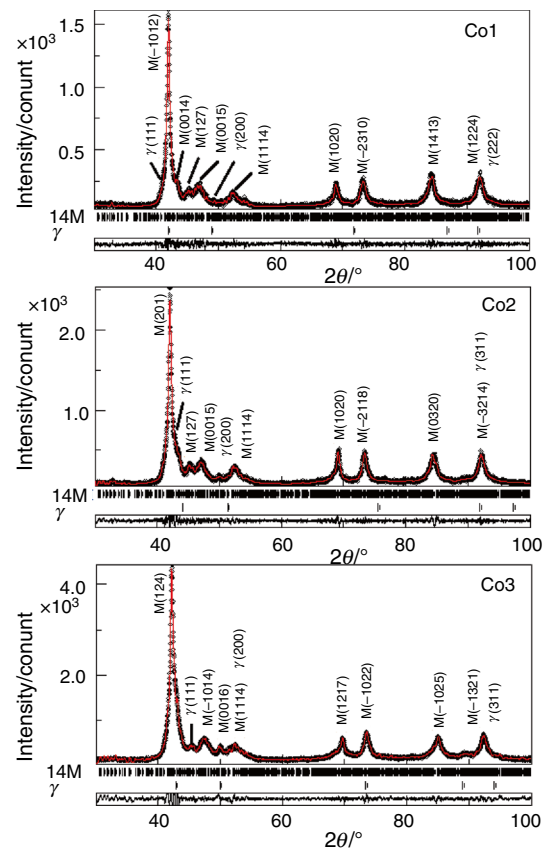

Fig. 2 Rietveld refinement of the XRD patterns of the Co1, Co2, and Co3 Heusler alloys

crystallographic considerations, the arrangement of atoms in the lattice, and magnetic interactions that stabilize it, leading to the coexistence of multiple phases. The occurrence of the *fcc* structure may be advantageous within certain temperature intervals and alloy compositions. Hence, the coexistence of the γ phase alongside the modulated 14M martensite in the Co-doped Ni–Mn–In Heusler alloys can be related to the complex interplay of various factors, including composition, temperature, and the underlying thermodynamics and kinetics of the phase transformations. The crystal structure of the $Ni_{40}Co_{10}Mn_{41+x}In_{9-x}$ ($x = 0, 2,$ and 4) Heusler alloys, manufactured by arc melting and subsequent annealing at 900°C for 24 h, consists of a tetragonal martensite and *fcc* γ phase [26]. For the martensite phase, the parameter a value decreased, and the parameter c value increased with reducing In content. Meanwhile, the parameter a value of the γ phase remained unchanged and comparable to those of biphasic Ni–Mn–Ga-based alloys [27]. In the case of the $Mn_{50}Ni_{40-x}In_{10}Co_x$ alloys ($x = 0, 1, 2,$ and 3) ingots prepared by arc melting, the crystal structure of Co0 and Co1 alloys consisted of body-centered tetragonal non-modulated martensite, a mixture of bcc austenite and tetragonal martensite

Table 1 Structure, lattice parameters (*a*, *b*, and *c*), *β* angle, average crystallite size (⟨*L*⟩) mass fraction, fit factors (Sig, and R_{wp}) of $(Ni_{50}Mn_{40}In_{10})_{100-x}Co_x$ alloys

Sample	Phase	a/nm $\pm 10^{-4}$	b/nm $\pm 10^{-4}$	c/nm $\pm 10^{-4}$	β (°)	⟨L⟩/nm ± 2	mass %	Sig	R_{wp}/%
Co0	*14M*	0.4262	0.5692	2.9276	92.98	79.4	100	1.11	11.83
Co1	*14M*	0.4302	0.5664	2.922	92.66	50.0	92.2		
	γ	0.3717	0.3717	0.3717	90.00	11.0	07.8	1.11	12.11
Co2	*14M*	0.4323	0.5618	2.912	92.71	88.0	74.8		
	γ	0.3559	0.3559	0.3559	90.00	16.0	25.2	1.20	9.28
Co3	*14M*	0.4352	0.5282	2.9246	93.00	98.0	60.4		
	γ	0.3645	0.3645	0.3645	90.00	09.0	39.6	1.06	12.22
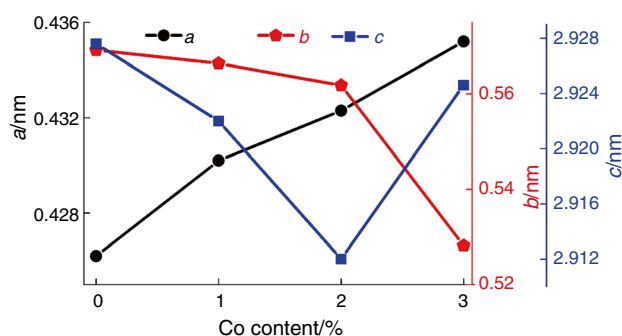
Fig. 3 Variation in the lattice parameters (*a*, *b*, and c) as a function of the cobalt content

for the Co2 alloy, and a pure austenite structure for the Co3 alloy [28].

The average crystallite size ranges from 50 to 98 nm for the 14M martensite structure and between 9 and 16 nm for the *γ* phase. Those nanosized crystallite sizes might be related to the melt-spinning process. The mass fraction of the *γ* phase increases with increasing the Co content; It is about 7.8%, 25.2%, and 39.6% for the Co1, Co2, and Co3 ribbons, respectively.

For the Co-free ribbons, the lattice parameters *a* = 0.4262 nm, *b* = 0.5692 nm, and *c* = 292.76 nm are comparable to those reported for the $Ni_{50}Mn_{50-x}In_x$ alloys [29]. The lattice parameter, *a*, of the 14M martensite augmented nearly linearly with the rise in the cobalt content, *b* decreased, and *c* decreased up to 2% Co and then increased (Fig. 3). The crystalline parameter *a* of the *γ* phase decreases from 0.3717 to 0.3559 nm, and then rises to 0.3645 nm for the Co1, Co2, and Co3, respectively. The obtained values differ from the reported ones for the $Ni_{40}Co_{10}Mn_{41+x}In_{9-x}$ (*x* = 0, 2, and 4), where *a* remains nearly constant at about 0.365–0.366 nm [26]. Those differences can be related to the preparation conditions.

Morphology of the ribbons

Secondary electrons (SE) images at different magnifications of the surface and cross-section (CS) of the Co1, Co2, and Co3 ribbons show the lamellar microstructure typical of martensite structure having variant orientations, alongside fine inclusions (small spherical grains and other shapes) with dark contrast that can be related to the secondary *γ* phase in addition to precipitates that can be related to a secondary phase, confirming thus the XRD results. The precipitates are distributed non-uniformly inside the grains and at the grain boundaries. Figure 4b shows an enlargement of Fig. 4a. The formation of some granules (and cavities) associated with local in homogeneities in the final stages of solidification of the ribbons is detected. Some micrographs (Fig. 4e) show that the martensitic structure is not observed in the whole ribbon because the elemental composition is about 60.6% Mn, 18.99%Ni, and 20.41%In. According to the micrographs of the cross sections, two effects are observed. On the one hand, the non-homogeneity in the thickness of the ribbons is due to the complex flow of the molten metal alloy and its impact on the surface of the rotating wheel. On the other hand, the formation of columnar crystals in the direction perpendicular to the surface of the ribbon (which coincides with the direction of crystallization).

Figure 5 displays the XRF spectra of the Co1, Co2, and Co3 Heusler alloys, indicating the presence of all the starting Ni, Mn, In, and Co elements. The analysis reveals that the Ni content fluctuates from 49.58 to 50.23 at.%, Mn varies between 38.67 and 39.32 at.%, In ranges between 8.76 and 9.46 at.%, and Co swings between 0.99 and 2.96 at.% (Table 2). One notes that the Ni content increases and the In content decreases, while that of Mn exhibits slight fluctuation for all samples compared to the starting nominal compositions. The observed deviations may arise from inherent heterogeneities in the as-cast ribbons or possibly from the evaporation of Mn or In during the melting process due to their lower evaporation enthalpies compared to Ni (ΔH_{Mn} (226 kJ mol^{-1}) < ΔH_{In} (232 kJ mol^{-1}) < ΔH_{Ni} (370 kJ mol^{-1})). The discrepancies in the atomic percentage

Fig. 4 Typical secondary electrons SEM micrographs of the free surface for melt-spun Co1 (**a**, **b**), Co2 (**c**, **d**), Co3 (**e**, **f**) ribbons, and the fracture cross-section (CS) at the bottom
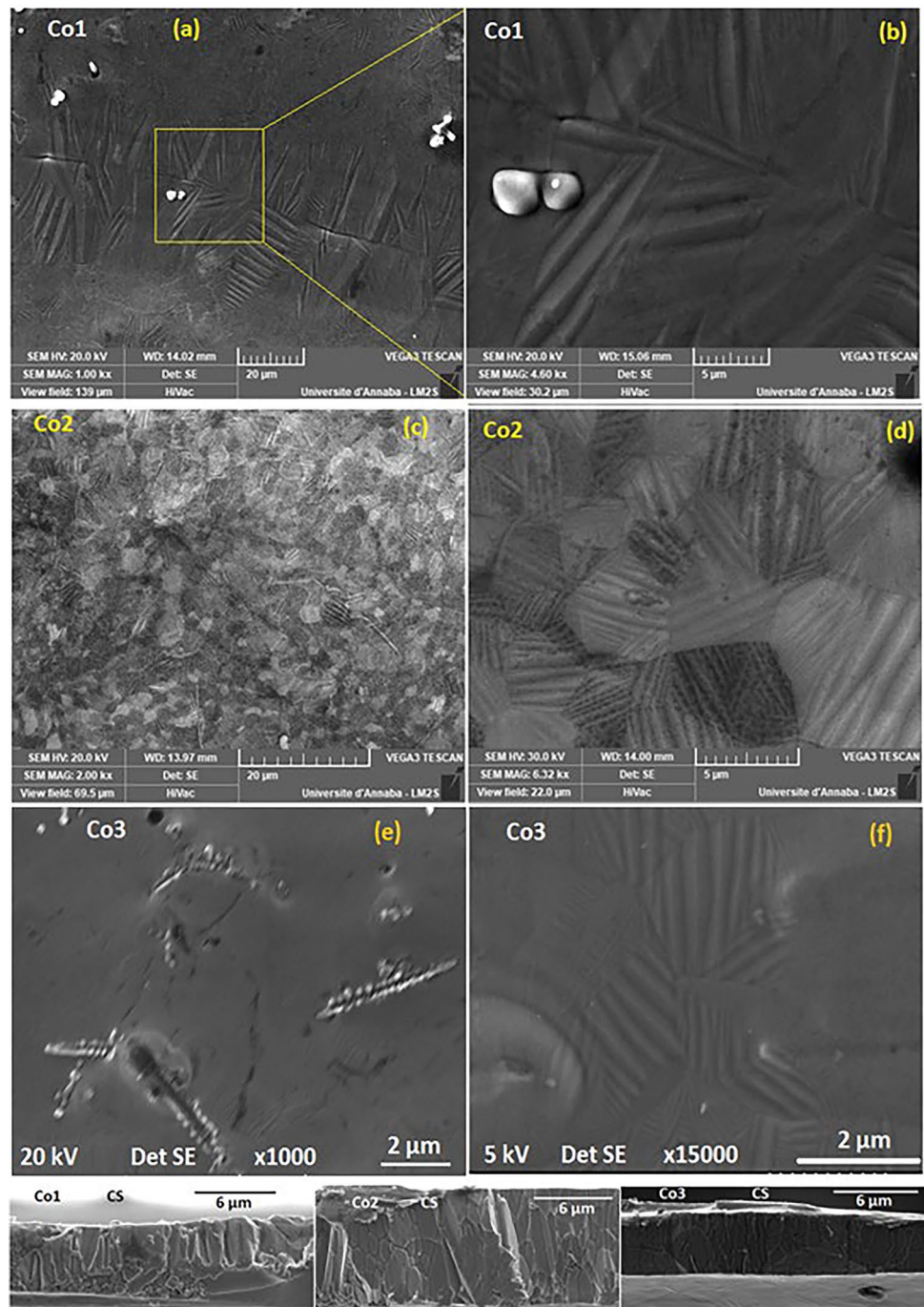
ratios for Ni, Mn, and In can impact the temperature of the martensitic transformation and the magnetic properties, which may be affected by several factors, including the *e/a* ratio, alloy's composition, atomic order degree, crystallite size, and Mn nearest neighbor interatomic distances [30, 31]. Additionally, the *e/a* ratio rises with increasing the cobalt content.

Energy-dispersive spectroscopy (EDS) was also used to assess the elemental composition of the Co1, Co2, and Co3

Heusler alloys. The results reveal the presence of two types of lamellae that differ by the indium content in their compositions. The lamellae with higher In content can be related to the Heusler matrix, while those with smaller amounts of In can be attributed to the γ phase. The light and spherical grains (Fig. 4a) are Mn-rich with approximately 98.8 at.% Mn. In Fig. 4b, the elemental composition of the matrix reveals that Ni, Mn, and In contents are approximately 49.24%, 39.5%, and 11.26%, respectively. The non-detection of the Co element
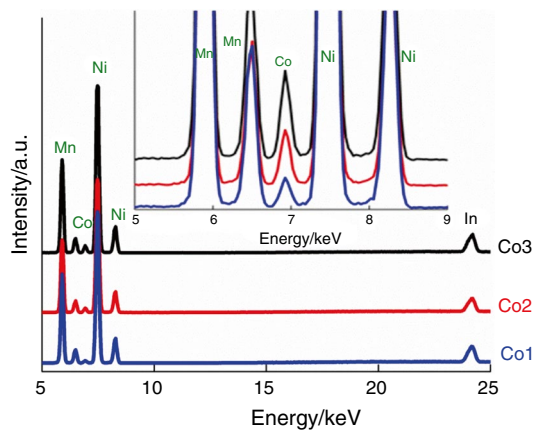
Fig. 5 Micro-ED-XRF spectra of Co1, Co2, and Co3 melt-spun ribbons

might be due to its smaller fraction and/or its substitution for Mn or Ni. The slight deviation from the nominal composition can be due to the heterogeneity of the ribbon compositions or loss of elements during the preparation of ingots by arc melting and the ribbons by melt-spinning processes. The electron-to-atom ratio (*e/a*) was ascertained by summing the *s*, *p*, and *d* electrons for Ni (10), Co (9), Mn (7), and In (3). The e/a ratio rises with the increase in the Co content.

Thermal analysis

The structural transformation from austenite to martensite is driven by the free energy excess, resulting from its great quantity of austenite compared to that of martensite. This transformation is well known by heat absorption/liberation, occurs with a reorganization of atomic positions, and the adopted final structure is consistent with the one with the lowest free energy. As the martensitic transition occurs in the diffusionless type, a thermal hysteresis appears during the martensite nucleation in addition to an increase in the elastic and surface energies. The DSC curves illustrate the occurrence of the martensitic phase transformation in the Co1 and Co2 Heusler alloys with an endothermic peak upon heating and an exothermic peak upon cooling at different heating rates of 3, 5, 7, and 10 °C min^{-1} (Fig. 6). Nevertheless, the DSC curves of the Co3 exhibit only an endothermic peak on heating for 7 °C min^{-1} ($A_{st} = 488.8$ °C and $A_f = 510.3$ °C) and 10 °C min^{-1} ($A_{st} = 512.86$ °C and $A_f = 524.92$ °C). The impediment of the forward martensitic transformation for the Co3 can be related

to various factors, such as the deviation of the alloy composition from stoichiometry, thermodynamic stability of the martensitic phase relative to the austenitic phase, the presence of kinetics barriers, and limitations in atom mobility during cooling. Moreover, structural defects, impurities, and secondary phases may obstruct the martensitic transformation on cooling. Accordingly, the non-occurrence of the forward martensitic transition can be ascribed to internal stains and the large lattice distortion of the 14M martensite compared to that of the Co-free ribbons (Table 1). Indeed, the relative deviation of the lattice parameters $\Delta a = \frac{a_{Co3} - a_{Co0}}{a_{Co0}}, \Delta b = \frac{b_{Co3} - b_{Co0}}{b_{Co0}}$, and $\Delta c = \frac{c_{Co3} - c_{Co0}}{c_{Co0}}$ reaches as much as $\Delta a = 2.11\%, \Delta b = -7.20\%$, and $\Delta c = -0.10\%$. Furthermore, the suppression of the reverse transformation might be related to the amount and microstructure of the γ phase with coarse grain morphology (Fig. 4e, f), random orientation, and distribution which are different from those of Co1 and Co2 ribbons.

The reverse and forward transformation temperatures were obtained by assessing the onset point of a baseline and the tangents to individual DSC peaks. M_{st} and M_f denote the onset and end points of the martensitic phase transformation, while A_{st} and A_f represent the austenite start and austenite finish temperatures, respectively. All the characteristic temperatures of the thermal hysteresis are summarized in Table 3. The phase transition region is characterized by equivalent martensite and austenite Gibbs energies at the equilibrium temperature (T_0), as well as thermodynamic parameters of the entropy (ΔS) and free energy (ΔG) given by the following relationships:

$$T_0 = \frac{M_{st} + A_f}{2} \tag{1}$$

$$\Delta S = \int_{T_2}^{T_1} \left[\frac{1}{T} \left(\frac{dQ}{dt} \right) \left(\frac{dT}{dt} \right)^{-1} \right] dT \tag{2}$$

$$\Delta G^x = \Delta H - T_s \Delta S \tag{3}$$

where the temperatures T_1 and T_2 are the limits of integration, Q is the heat exchange during the transformation and identified by the enthalpy change (ΔH) that corresponds to the total area under the exothermic and endothermic peaks, and T_s is the starting temperature of each process example M_{st} for the direct transition and A_{st} for the reverse one. The

Table 2 Micro-ED-XRF analysis of $(Ni_{50}Mn_{40}In_{10})_{100-x}Co_x$ ($x = 1$, 2, and 3) melt-spun ribbons

Sample	Ni/at.%	Mn/at.%	In/at.%	Co/at.%	e/a/exp	e/a/Theo
Co1	50.23	39.32	9.46	0.99	8.148	8.109
Co2	49.93	39.31	8.76	2.00	8.194	8.118
Co3	49.58	38.67	8.79	2.96	8.148	8.127

Fig. 6 DSC scans during the heating/cooling processes at different rates for the Co1 (**a**, **b**), Co2 (**c**, **d**), Co3 (**e**) and with a heating rate of 10 °C min^{-1} for the Co1, Co2, and Co3 ribbons (**f**)
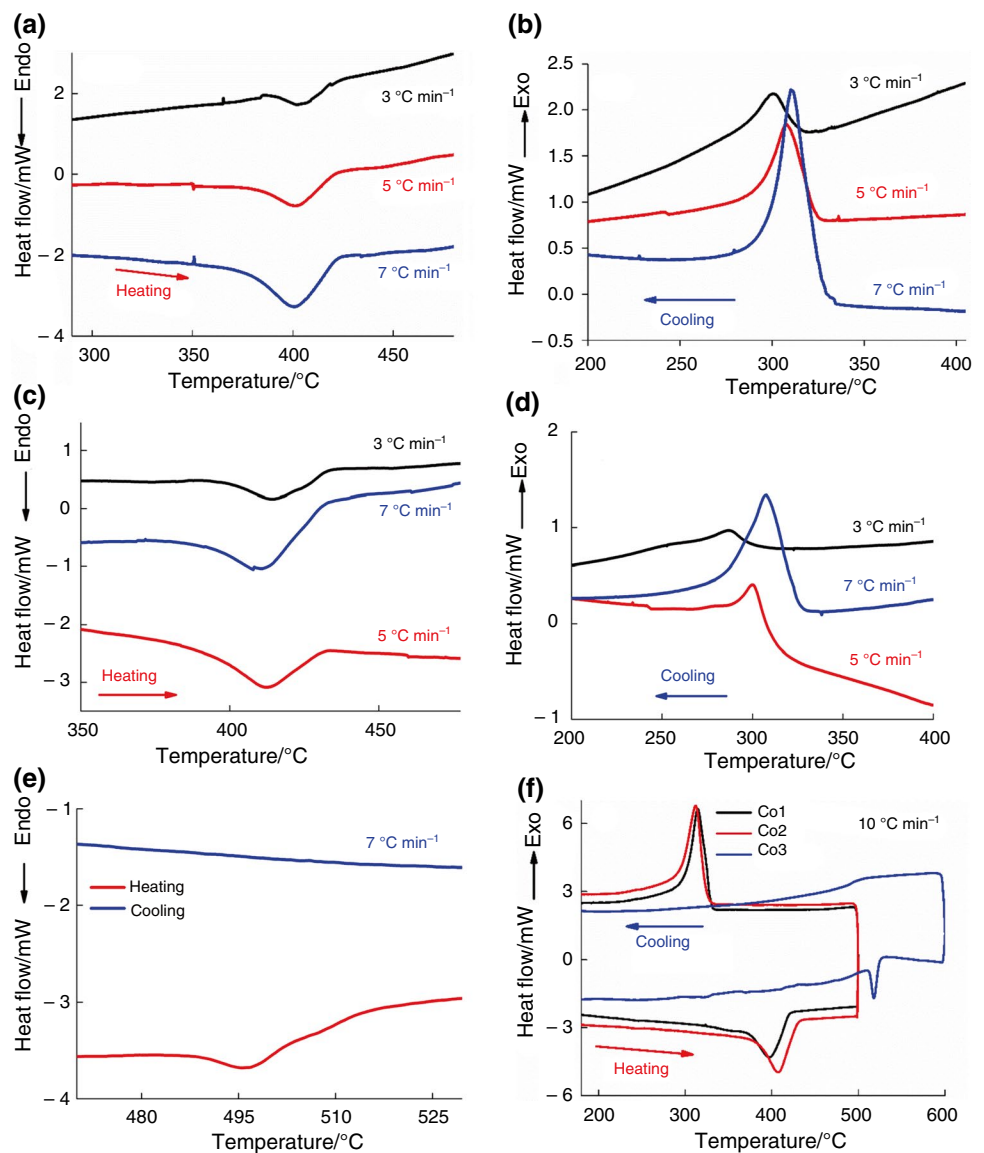
heat exchange (Q) is roughly equal to the enthalpy change of a transformation [32]. They differ by the elastic energy (E_{el}) and irreversible dissipated energy (W_d) contributions defined as:

$$Q = \int_{M_{st}/A_s}^{M_f/A_f} T \cdot dS = \Delta H - E_{el} + W_d \qquad (4)$$

The relative fractions of the elastic and dissipated energies concerning the total transformation enthalpy ($E_{el}/\Delta H$ and $W_d/\Delta H$) can be determined using the average value of enthalpy between the cooling and heating processes according to the following equations:

$$E_{el} = \frac{1}{4}\Delta S[(A_f - A_{st}) + (M_{st} - M_f)] \qquad (5)$$

$$W_d = \frac{1}{2}\Delta S[(A_f + A_{st}) - (M_{st} + M_f)] \qquad (6)$$

The thermodynamic parameters of the thermal hysteresis temperature (ΔT_{hys}), enthalpy (ΔH), entropy (ΔS), free energy (ΔG), and the relative fractions of the elastic and dissipated energies ($E_{el}/\Delta H$ and $W_d/\Delta H$) are gathered in Table 3. The Co1 and Co2 samples show a martensitic transformation overhead room temperature (RT). The thermal hysteresis displays an endothermic peak on heating and an exothermic peak on cooling. Moreover, the height of endothermic and exothermic peaks increases as the heating/cooling rate increases. Consequently, the area under the endothermic and exothermic peaks of the Co1 alloy changes, respectively, from 0.5 to 2.4 J g^{-1} and from 1.4 to 3.9 J g^{-1}. However, for the Co2 alloy, the area under the endothermic and exothermic peaks increases when the heating/cooling

Table 3 The measured characteristic transformation temperatures (A_s, A_f, M_s, and M_f) and the calculated thermodynamic parameters (ΔT_{hys}, ΔH, ΔS, ΔG, $E_{el}/\Delta H$, $W_d/\Delta H$, and Ea)

Thermodynamic parameters	Co1				Co2			
	Heating/cooling rate/°C min^{-1}				Heating/cooling rate/°C min^{-1}			
	3	5	7	10	3	5	7	10
A_s/°C	388	351	352	359.7	383	300	338	368.23
A_f/°C	442	469	467	422.6	440	455	451	426.22
M_{st}/°C	312	357	350	329.8	371	385	342	327.08
M_f/°C	203	150	165	295.5	163	160	155	291.48
ΔT_{hys}/°C	157	156	152	78.5	144	105	146	87.94
ΔH/J g^{-1}								
Heating	0.52	2.37	0.88	36.74	2.91	2.98	2.98	32.50
Cooling	1.44	3.15	1.64	35.33	4.37	3.42	3.42	36.38
ΔS/J kg^{-1} K^{-1}								
Heating	0.8	3.4	1.3	58.12	4.2	4.4	4.4	51.43
Cooling	2.2	4.6	2.4	55.88	6.3	5.1	5.1	57.57
ΔG/J kg^{-1}								
Heating	0.8	214.6	29.2	34	504.7	260.9	260.9	48
Cooling	144.3	257.7	83.8	3551	221	279.1	279.1	3878
$E_{el}/\Delta H$/%	6.3	11.8	0.8	3.84	3.84	13.7	11.2	3.70
$W_d/\Delta H$/%	48.5	22.7	1.6	6.94	6.94	15.5	21.8	13.91
Eq/kJ mol^{-1}	257				135.6			

rate equals 5 °C min^{-1} and then decreases. This decrease might be linked to the local composition heterogeneities as the thermal analysis was studied using a small quantity of samples. In general, an increase in ΔH with the heating rate can be related to several types of structural defects, mainly dislocations, which cause inner stress [33]. Furthermore, the entropy increases as the scan rate rises from 3 to 7 °C min^{-1}, which can be correlated to the increase in the atomic disorder degree.

The martensitic transformation temperature can be significantly changed by the electron-to-atom ratio (e/a), atomic order degree, Mn–Mn interatomic distances, and crystallite size [34]. Meanwhile, it increases with the e/a ratio for several NiMn-based Heusler alloys [35], but our results show an opposite trend. The martensitic transformation temperature increases with increasing the cobalt proportion and decreasing e/a ratio from 8.02 for the Co1 alloy to 7.94 for the Co2 alloy. This increase can be correlated to the $d_{Mn} - d_{Mn}$ interatomic distance change after the cobalt addition. One can also mention that for the initial composition (ribbons of Ni$_{50}$Mn$_{40}$In$_{10}$, e/a = 8.13) [29], the characteristic structural temperatures are lower than the found ones in this study. Indeed, Heusler alloys' structural transition temperatures are sensitive to composition modification and e/a change [36]. The martensitic transition onset (M_{st}) slightly shifts toward upper temperatures by surging the scan rate due to the thermally activated character. However, the M_f diminishes with the increase in both the cooling rate and cobalt content. It was reported that the martensitic transition temperatures are

not responsive to feeble rates until they reach 10 K min^{-1}, showing a decrease by raising the heating/cooling rate [37].

It is believed that different orientation of the formed martensitic variants influences the equilibrium temperature T_0 values, which increase by increasing the Co content. Furthermore, T_0 has no monotonic tendency with the scan speed increase. The width of the thermal hysteresis, defined as $\Delta T_{hys} = \frac{A_{st}+A_f}{2} - \frac{M_{st}+M_f}{2}$, is an efficient criterion to describe the structural transformation. Changing the composition namely the electron-to-atom ratio and $d_{Mn} - d_{Mn}$ interatomic distances leads to a decrease in ΔT_{hys} values. During the structural transition, the stored elastic energy is used as a driving force. The enthalpy fraction remaining in the system as elastic energy is less than 12% for the Co1 and 14% for the Co2 which consistently varies with T_0. At the thermodynamic equilibrium ($\Delta G = 0 = \Delta H - T_0\Delta S$), a decrease in T_0 temperature ($T_0 = \frac{\Delta H}{\Delta S}$) can be linked to a decrease in ΔH or an increase ΔS. The enthalpy fraction linked to the dissipated energy has higher values for the Co1 sample.

Kissinger-like methods [38] are usually used to determine the apparent activation energy in thermally activated mechanisms. Several studies showing a first-order transformation, particularly for Heusler alloys [39, 40], were based on calorimetric results comparing calculated phenomenological parameters with the literature, such as the activation energy. The Kissinger relation ($\mathrm{Ln}\left(\frac{\beta}{T^2}\right) = \frac{-E_a}{RT} + c$) can be verified through the linearity

of $\text{Ln}\left(\frac{\beta}{T^2}\right)$ against the $1/T$ plot, where β is the scanning rate, T is the transition peak temperature, E_a is the activation energy, R is the perfect gas constant, and c is a constant coefficient. The linear fit of $\text{Ln}\left(\frac{\beta}{T^2}\right)$ vs. T^{-1} plot is depicted in Fig. 7. The activation energy value decreases from $E_a = 257$ kJ mol^{-1} for the Co1 to $E_a = 135.6$ kJ mol^{-1} for the Co2. The decrease in the activation energy with the increase in the Co content may be ascribed to the relatively easy growth of the martensite due to the drop of the barrier height required for the reverse martensitic as phase transformation occurs. This decrease can be related to the increase in the mass fraction of the γ phase for the Co2 ribbons and the reduction in thermal stability and lowering of the resistance to crystallization in the Co-doped Heusler alloys. A comparable crystallization activation energy value to that of the Co1 ribbons was reported to be $E_a \sim 239 \pm 19$ kJ mol^{-1} for the amorphous Ni$_{50}$Mn$_{38}$Co$_6$In$_6$ films [41]. The activation energies of the transition processes B2 to L21 and Mn to MnNi in the mechanically alloyed Ni$_{45.5}$Co$_{4.5}$Mn$_{36.6}$In$_{13.4}$ powders were calculated as 185(6) kJ mol^{-1} and 228(3) kJ mol^{-1}, respectively [42].

Magnetic measurements

Figure 8 shows the hysteresis loops of Co1, Co2, and Co3 alloys at room temperature, subject to both the applied magnetic field perpendicular (per) field to the ribbon plane and along the ribbon length (par). The paramagnetic behavior in the Co-doped Heusler alloys can be related to the atomic disorder in the melt-spun ribbons. Moreover, the hysteresis loops manifest a negative shift along the horizontal H-axis and a positive shift along the vertical M-axis. The horizontal translation of the hysteresis loop on the H-axis is linked to the emergence of a magnetically non-uniform antiferromagnetic (AFM)/ferromagnetic (FM) matrix due to the interfacial pinning of FM spins by the AF component, resulting in an exchange bias (EB) behavior. The exchange bias is often associated with interactions at the interfaces between different magnetic phases, leading to the creation of exchange
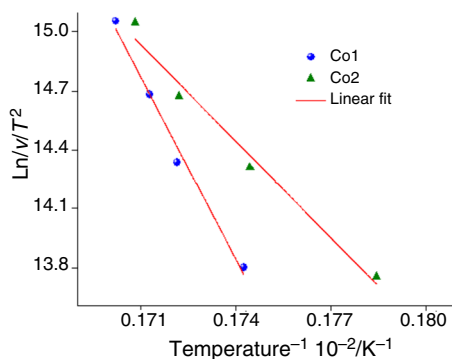
anisotropy at the interface between AFM and FM regions related to the development of a unidirectional ferromagnetic anisotropy (texture) at the interface between different magnetic phases during the formation of the ribbons. As revealed by the EDS analysis, the prepared ribbons exhibit a heterogeneous elemental composition with Mn-rich lamellae and grains.

The FM-AFM interactions in the off-stoichiometric alloys can be related to the AFM coupling between Mn atoms in their regular sites and those occupying Z sites. A similar finding was observed in the Ni$_{51.82}$Mn$_{32.37}$In$_{15.81}$ melt-spun ribbons [29]. The variation in the coercivity and exchange bias as a function of the cobalt content is illustrated in Fig. 9. The coercivity reaches a maximum value for the Co2 and a minimum value for the Co3 if the applied magnetic field is parallel or perpendicular. The variation in the coercivity exhibits the same tendency as those of the crystallite size and mass fraction of the γ phase (inset in Fig. 9). The reduction in the exchange bias effect with the increase in the Co content can be due to several factors, including microstructural changes, atomic disorder at the atomic level that can affect the alignment of magnetic moments and magnetic interactions, alter the arrangement of magnetic domains which can affect the formation of magnetic interfaces and modify the nature of the interfacial interactions.
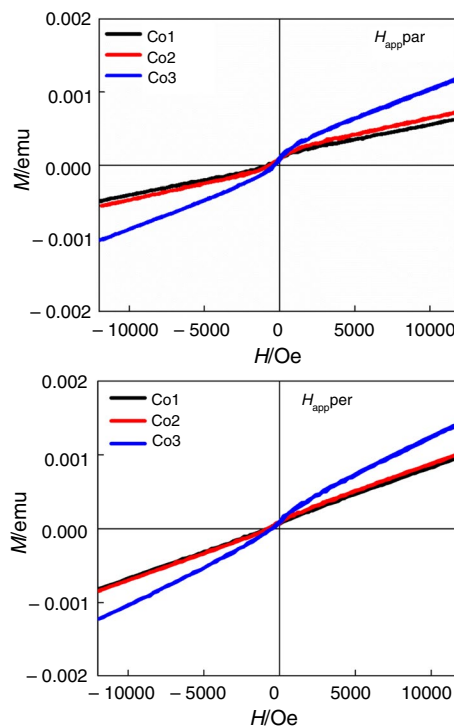

Fig. 7 Kissinger's plots of for the Co1 and Co2 ribbons

Fig. 8 Hysteresis loops of the Co1, Co2, and Co3 ribbons under a parallel (par) and perpendicular (per) applied magnetic fields
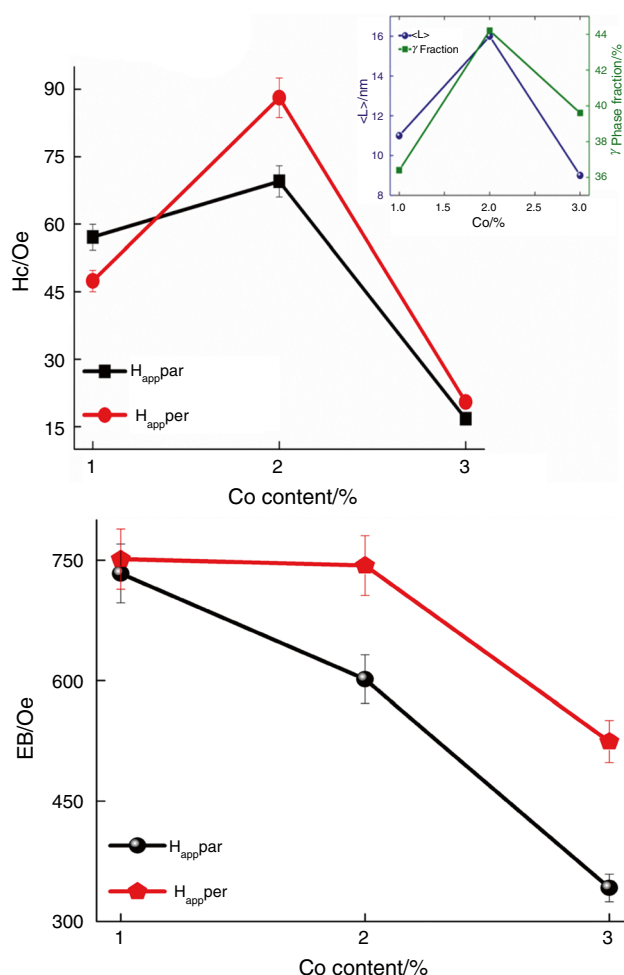
Fig. 9 Variations in the coercivity and exchange bias as a function of the cobalt content

Conclusions

Cobalt element is successfully doped in $(Ni_{50}Mn_{40}In_{10})_{100-x}Co_x$ ($x = 1, 2,$ and 3) alloys. The XRD results reveal the formation of a 14M martensite structure alongside the *fcc* g phase. The lattice constant of the g phase varies between 0.3559 and 0.3717 nm, and its mass fraction reaches a maximum value for the Co2 alloy. The increase in the Co content decreases the activation energy value and the forward transition temperatures and increases the reverse transformation temperatures (Ast and Af). The highest and lowest coercivity values were obtained for the Co2 and Co3 ribbons, respectively. The exchange bias decreases as the Co content increases.

Declarations

Conflict of interest The authors declare no conflict of interest.

References

1. Tavares S, Yang K, Meyers MA. Heusler alloys: past, properties, new alloys, and prospects. Prog Mater Sci. 2023. https://doi.org/10.1016/j.pmatsci.2022.101017.
2. Samanta S, Ghosh S, Mandal K. Observation of giant exchange bias effect in Ni–Mn–Ti all-d-metal Heusler alloy. J Phys: Cond Mater. 2021. https://doi.org/10.1088/1361-648X/ac3e9b.
3. Załęski K, Ekholm M, Alling B, Abrikosov IA, Dubowik J. Local atomic configuration approach to the nonmonotonic concentration dependence of magnetic properties of $Ni_2Mn_{1+x}Z_{1-x}$ ($Z = In,$ Sn, Sb) Heusler alloys. Scr Mater. 2021. https://doi.org/10.1016/j.scriptamat.2020.113646.
4. Sharma J, Suresh KG, Raja MM, Walke P. Martensitic transition, magnetic, microstructural and exchange bias properties of melt spun ribbons of Mn–Ni–Sn shape memory Heusler alloy. Front Mater. 2020. https://doi.org/10.3389/fmats.2020.520630.
5. Elphick K, Frost W, Samiepour M, Kubota T, Takanashi K, Sukegawa H, Mitani S, Hirohata A. Heusler alloys for spintronic devices: review on recent development and future perspective. Sci Technol Adv Mater. 2021;22(1):235–71. https://doi.org/10.1080/14686996.2020.1812364.
6. Dadda K, Alleg S, Suñol JJ, Bessais L, Hlil EK. Structure, magnetocaloric effect and critical behaviour in $Ni_{50}Mn_{30}(Sn, In)_{20}$ Heusler alloys. J Supercond Nov Magn. 2020;33:2209–18. https://doi.org/10.1007/s10948-020-05485-3.
7. Kaletina YuV, Gerasimov EG. Martensitic transformations and magnetic properties of nonstoichiometric alloys of the Ni–Mn–In system. Phys Solid State. 2014. https://doi.org/10.1134/S1063783414080101.
8. Chen F, Llamazares JS, Sánchez-Valdés CF, Chen F, Li Z, Tong YX, Li L. Large magnetic entropy change and refrigeration capacity around room temperature in quinary $Ni_{41}Co_{9-x}Fe_xMn_{40}Sn_{10}$ alloys (x = 20 and 25). J Alloys Compd. 2020;825:154053. https://doi.org/10.1016/j.jallcom.2020.154053.

9. Pal D. Conventional and inverse magnetocaloric effect in Ni-rich Ni–Mn–Ga and Ni–Mn–Sn Heusler alloy: a comparison. J Sci Res. 2020. https://doi.org/10.3329/jsr.v12i3.44357.

10. Camarillo-Garcia JP, Hernández-Navarro F, Flores-Zúñiga H, Baltazar-Hernandez VH, Alvarado-Hernández F. Contrasting response on magnetocaloric effect and refrigeration capacity due to Ni or Mn substitution by Fe in Ni–Mn–In–Co–Fe alloys. J Alloys Compd. 2023. https://doi.org/10.1016/j.jallcom.2022.167852.

11. Kamantsev AP, Koshkidko YS, Bykov EO, Gottschall T, Gamzatov AG, Aliev AM, Kameli P. Giant irreversibility of the inverse magnetocaloric effect in the $Ni_{47}Mn_{40}Sn_{12.5}Cu_{0.5}$ Heusler alloy. Appl Phys Lett. 2023. https://doi.org/10.1063/5.0176772.

12. Sepehri-Amin H, Taubel A, Ohkubo T, Skokov KP, Gutfleisch O, Hono K. Microstructural origin of hysteresis in Ni–Mn–In based magnetocaloric compounds. Acta Mater. 2018. https://doi.org/10.1016/j.actamat.2018.01.044.

13. Feng Y, Chen H, Xiao F, Bian X, Wang P. Improvement of mechanical property and large shape recovery of sintered $Ni_{45}Mn_{36.6}In_{13.4}Co_5$ alloy. J Alloys Compd. 2018;765:264–70. https://doi.org/10.1016/j.jallcom.2018.06.244.

14. Aksoy S. Synthesis and characterization of NiMnIn nanoparticles. J Magn Magn Mater. 2015. https://doi.org/10.1016/j.jmmm.2014.04.003.

15. Coll R, Saurina J, Escoda L, Sunol JJ. Thermal analysis of $Mn_{50}Ni_{50-x}(Sn, In)_x$ Heusler shape memory alloys. J Therm Anal Calorim. 2018. https://doi.org/10.1007/s10973-018-7551-x.

16. Ghahremani M, Aslani A, Hosseinnia M, Bennett LH, Della TE. Direct and indirect measurement of the magnetocaloric effect in bulk and nanostructured Ni–Mn–In Heusler alloy. AIP Adv. 2018. https://doi.org/10.1063/1.5007223.

17. Liu J, Scheerbaum N, Kauffmann-Weiss S, Gutfleisch O. NiMn-based alloys and composites for magnetically controlled dampers and actuators. Adv Eng Mater. 2012. https://doi.org/10.1002/adem.201200038.

18. Pathak AK, Dubenko I, Pueblo C, Basnyat P, Stadler S, Ali N. The effect of partial substitution of Ni by Co on the magnetic and electrical properties of $Ni_{50}Mn_{35}In_{15}$ Heusler alloy. IEEE Trans Magn. 2010. https://doi.org/10.1109/TMAG.2010.2043924.

19. Zhang W, Balasubramanian B, Ullah A, Pahari R, Li X, Yue L, Valloppilly SR, Sokolov A, Skomski R, Sellmyer DJ. Comparative study of topological Hall effect and skyrmions in NiMnIn and NiMnGa. Appl Phys Lett. 2019. https://doi.org/10.1063/1.5120406.

20. Porcar L, Miraglia S, Porcher F, Haettel R, Plaindoux P, Silveira Reis Perticarrari M, Dufour H, Pairis S, Jarreau J, Verdier M, Bourgault D. Long flexible melt-spun Ni–Co–Mn–In ribbons with shape memory effect and caloric perfomances above 300 K. Materialia. 2019;8:100493. https://doi.org/10.1016/j.mtla.2019.100493.

21. Ma T, Zhang K, Han B, Zhao L, Zhao W, Wang C, Tian X, Tan C. Dynamic control and increase of working temperature range in Ni–Mn–In–Co MCE materials by hydrostatic pressure or biaxial stress. Mater Today Commun. 2022. https://doi.org/10.1016/j.mtcomm.2022.104051.

22. Karaca HE, Karaman I, Basaran B, Ren Y, Chumlyakov YI, Maier HJ. Magnetic field-induced phase transformation in NiMnCoIn magnetic shape-memory alloys—a new actuation mechanism with large work output. Adv Funct Mater. 2009. https://doi.org/10.1002/adfm.200801322.

23. Paramanik T, Das I. Near room temperature giant magnetocaloric effect and giant negative magnetoresistance in Co, Ga substituted Ni–Mn–In Heusler alloy. J Alloys Compd. 2016;654:399–403.

24. Kihara T, Xu X, Ito W, Kainuma R, Tokunaga M. Direct measurements of inverse magnetocaloric effects in metamagnetic shape-memory alloy NiCoMnIn. Phys Rev B. 2014. https://doi.org/10.1103/PhysRevB.90.214409.

25. Lutterotti L. Maud: a Rietveld analysis program designed for the internet and experiment integration. Acta Cryst. 2000. https://doi.org/10.1107/S0108767300021954.

26. Yang S, Wang C, Shi Z, Wang J, Zhang J, Huang Y, Liu X. Microstructure, martensitic transformation, mechanical and shape memory properties of Ni–Co–Mn–In high-temperature shape memory alloys under different heat treatments. Mater Sci Eng A. 2016. https://doi.org/10.1016/j.msea.2015.12.091.

27. Ma Y, Yang S, Liu Y, Liu X. The ductility and shape-memory properties of Ni–Mn–Co–Ga high-temperature shape-memory alloys. Acta Mater. 2009. https://doi.org/10.1016/j.actamat.2009.03.025.

28. Wu Z, Liu Z, Yang H, Liu Y, Wu G. Effect of Co addition on martensitic phase transformation and magnetic properties of $Mn_{50}Ni_{40-x}In_{10}Co_x$ polycrystalline alloys. Intermet. 2011. https://doi.org/10.1016/j.intermet.2011.08.001.

29. Dadda K, Alleg S, Saurina J, Escoda L, Suñol JJ. Structure, microstructure, and magnetic properties of melt spun $Ni_{50}Mn_{50-x}In_x$ Ribbons. Magnetochemistry. 2021;1:23–204. https://doi.org/10.3390/magnetochemistry7050063.

30. Kustov S, Corró ML, Pons J, Cesari E. Entropy change and effect of magnetic field on martensitic transformation in a metamagnetic Ni–Co–Mn–In shape memory alloy. Appl Phys Lett. 2009. https://doi.org/10.1063/1.3130229.

31. Recarte V, Pérez-Landazábal JI, Sánchez-Alarcos V, Rodríguez-Velamazán JA. Dependence of the martensitic transformation and magnetic transition on the atomic order in Ni–Mn–In metamagnetic shape memory alloys. Acta Mater. 2012. https://doi.org/10.1016/j.actamat.2012.01.020.

32. Quintana-Nedelcos A, Llamazares JS, Ríos-Jara D, Lara-Rodríguez AG, García-Fernández T. Effect of quenching rate on the average grain size and martensitic transformation temperature in rapidly solidified polycrystalline $Ni_{50}Mn_{37}Sn_{13}$ alloy ribbons. Phys Stat Sol A. 2013. https://doi.org/10.1002/pssa.201329146.

33. Krenke T, Moya X, Aksoy S, Acet M, Entel P, Mañosa LI, Planes A, Elerman Y, Yücel A, Wassermann EF. Electronic aspects of the martensitic transition in Ni–Mn based Heusler alloys. J Magn Magn Mater. 2007. https://doi.org/10.1016/j.jmmm.2006.10.1139.

34. Zheng H, Wang W, Xue S, Zhai Q, Frenzel J, Luo Z. Composition-dependent crystal structure and martensitic transformation in Heusler Ni–Mn–Sn alloys. Acta Mater. 2013. https://doi.org/10.1016/j.actamat.2013.04.035.

35. Brzoza A, Wierzbicka-Miernik A, Czeppe T, Cesari E, Szczerba MJ. Composition dependence of martensitic transformation and crystal structure in $Ni_{50}Mn_{25}Ga_{25-x}Cu_x$ Heusler alloys. Intermet. 2019. https://doi.org/10.1016/j.intermet.2019.03.019.

36. Bachaga T, Zhang J, Ali S, Sunol JJ, Khitouni M. Impact of annealing on martensitic transformation of $Mn_{50}Ni_{42.5}Sn_{7.5}$ shape memory alloy. Appl Phys A. 2019;1:3–111. https://doi.org/10.1007/s00339-019-2389-z.

37. Kissinger HE. Reaction kinetics in differential thermal analysis. Anal Chem. 1957. https://doi.org/10.1021/ac60131a045.

38. Malinov S, Guo Z, Sha W, Wilson A. Differential scanning calorimetry study and computer modeling of $\beta \Rightarrow \alpha$ phase transformation in a Ti–6Al–4V alloy. Metal Mater Trans A. 2001. https://doi.org/10.1007/s11661-001-0345-x.

39. Zheng H, Wu D, Xue S, Frenzel J, Eggeler G, Zhai Q. Martensitic transformation in rapidly solidified Heusler $Ni_{49}Mn_{39}Sn_{12}$ ribbons. Acta Mater. 2011. https://doi.org/10.1016/j.actamat.2011.05.044.

40. Sánchez-Alarcos V, Pérez-Landazábal JI, Gómez-Polo C, Recarte V. Influence of the atomic order on the magnetic characteristics of

a Ni–Mn–Ga ferromagnetic shape memory alloy. J Magn Magn Mater. 2008. https://doi.org/10.1016/j.jmmm.2008.02.039.

41. Rios S, Karaman I, Zhang X. Crystallization and high temperature shape memory behavior of sputter-deposited Ni–Mn–Co–In thin films. Appl Phys Lett. 2010;1:23–45. https://doi.org/10.1063/1.3407670.

42. Rekik H, Hammami B, Khitouni M, Bachagha T, Suñol JJ, Chemingui M. Microstructure and kinetics of thermal behavior of martensitic transformation in (Mn, Ni)Sn Heusler alloy. Crystals. 2022. https://doi.org/10.3390/cryst12111644.

Publisher's Note Springer Nature remains neutral with regard to jurisdictional claims in published maps and institutional affiliations.